

## ARTICLE OPEN



## Broadband mechanoresponsive liquid metal sensors

Md Saifur Rahman<sup>1</sup>, Julia E. Huddy<sup>1</sup>, Andrew B. Hamlin<sup>1</sup> and William J. Scheideler<sup>1</sup>

Stretchable electronics have the fundamental advantage of matching the complex geometries of the human body, providing opportunities for real-time biomechanical sensing. We report a method for high-frequency AC-enhanced resistive sensing that leverages deformable liquid metals to improve low-power detection of mechanical stimuli in wearable electronics. The fundamental mechanism of this enhancement is geometrical modulation of the skin effect, which induces current crowding at the surface of a liquid metal trace. In combination with DC sensing, this method quantitatively pinpoints mechanical modes of deformation such as stretching in-plane and compression out-of-plane that are traditionally impossible to distinguish. Here we explore this method by finite element simulations then employ it in a glove to detect hand gestures and tactile forces as well as a respiratory sensor to measure breathing. Moreover, this AC sensor uses lower power (100X) than DC sensors, enabling a new generation of energy-efficient wearables for haptics and biomedical sensing.

npj Flexible Electronics (2022)6:71 ; <https://doi.org/10.1038/s41528-022-00206-3>

## INTRODUCTION

Stretchable electronics are uniquely matched to the complex geometries and compliant mechanics of human physiology. This capability allows stretchable and flexible devices to target various on-body biomedical sensing applications such as pulse wave sensing<sup>1</sup>, oximetry<sup>2</sup>, and bio-impedance tomography<sup>3</sup> due to their multidirectional stretchability and deformability. In addition, conformal contact provided by stretchable materials can enhance signal quality by reducing motion artifacts<sup>4</sup> and transforming wearable electronics into lightweight and unobtrusive devices that are virtually imperceptible<sup>5</sup>. Liquid metals such as the eutectic alloys of Ga and In (EGaIn) (75.5% Ga, 24.5% In) and Galinstan (68.5% Ga, 21.5% In, and 10.0% Sn)<sup>6</sup> are the highest performance materials available for stretchable electronic interconnects<sup>7,8</sup> due to their high electrical conductivity ( $3.4 \times 10^4 \text{ S cm}^{-1}$ ) and low toxicity. Furthermore, EGaIn's liquid state easily accommodates the cyclic loads of large uniaxial and biaxial strain required for wearable devices without requiring serpentine patterning<sup>9,10</sup>.

The reliability and performance of liquid metal conductors are of great importance to stretchable wireless circuits<sup>11</sup> that integrate many passive components, sensors, and ICs. These wearable systems will encounter deformation during regular use, including a biaxial strain of up to 30–40%<sup>12</sup> in the skin at joints such as the knuckles or elbow. Sustaining these mechanical deformations also allows resistive *sensing modalities* to turn liquid metal traces into strain gauges. The deformation of liquid metal flexible circuits can include modes such as mechanical stretching in-plane, torsion, and compression out-of-plane. While the electrical response of liquid metal conductors to many of these modes of mechanical deformation has been well-documented based on their DC resistance, which reflects the degree of strain, cross-sectional geometry, and length<sup>13</sup>, their high-frequency response to these modes has not yet been explored.

Modulation of AC resistance presents a promising modality that can expand the sensitivity and capabilities of liquid metal stretchable sensors by fully leveraging the physics of their deformable geometry. Past work in AC-based liquid metal sensing utilized time domain sensing via reflections on liquid metal transmission lines<sup>14</sup> as well as changes in inductance<sup>15</sup> or

capacitance<sup>16–18</sup>. However, these past works have not yet examined a key feature of liquid metals at higher frequencies above 1 MHz—which is that the deformable conductor cross-section naturally modifies their electromagnetics and changes the effective resistivity at the microscale. Understanding the electro-dynamics of AC conduction in liquid metal conductors is essential for designing sophisticated stretchable analog circuits for sensing and communication. Specifically, high-density stretchable electronics with passive components such as resistors, capacitors, vias, etc., made from liquid metal through soft lithography could greatly benefit from a study of high-frequency AC resistance response to mechanical deformation<sup>19–21</sup>. The AC performance is also a central question that underlies the use of liquid metals for applications such as wireless power transfer that are highly sensitive to resistive losses<sup>22</sup>. In this paper, we develop AC-based resistive sensing by exploiting the skin effect in deformable liquid metal conductors. We use this method to enhance the sensitivity of liquid metal mechanical sensors to distinguish both stretching (parallel to length) and compression (orthogonal to length) modes of deformation and to understand the origins of enhanced sensitivity with finite element electromagnetic (EM) simulations. Finally, we experimentally demonstrate AC resistive sensing in a wearable haptic glove device and a wearable respiratory sensing band, illustrating *multimodal* detection of both stretching and compression with low-power consumption.

## RESULTS AND DISCUSSION

At high frequencies (MHz–GHz), liquid metals exhibit the AC skin effect, as internal eddy currents force the majority of current to flow near the conductor's surface<sup>23</sup>. The current density decays exponentially from the surface according to an effective depth, skin depth ( $\delta$ ), given by the resistivity ( $\rho$ ), frequency ( $f$ ), and magnetic permeability ( $\mu$ ).

$$\delta = \sqrt{\frac{\rho}{\pi \cdot f \cdot \mu}} \quad (1)$$

The skin depth scales inversely with the conductivity of the metal, leading to a larger skin depth in Ga-based liquid metals due

<sup>1</sup>Thayer School of Engineering, Dartmouth College, Hanover, NH 03755, USA. ✉email: [william.j.scheideler@dartmouth.edu](mailto:william.j.scheideler@dartmouth.edu)

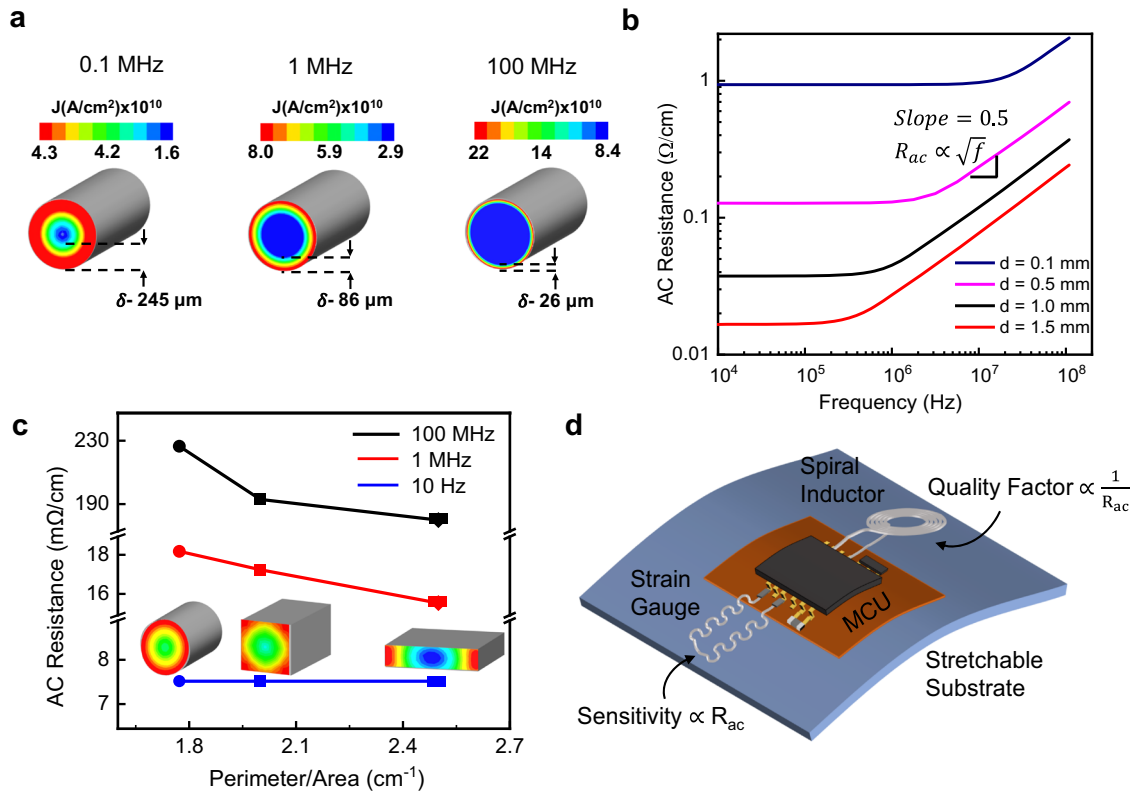


**Fig. 1** Finite element analysis simulated AC resistance for liquid metal-filled conductors for flexible electronics applications. **a** Current density maps illustrating simulated bulk vs. surface current crowding for low (100 kHz, left), medium (10 MHz, middle) and high (100 MHz, right) frequency signals. **b** Simulated AC resistance per length of liquid metal conductors of varying diameter as a function of frequency, indicating the positive power law scaling with frequency. **c** Simulated AC resistance of circular, square, and rectangular cross-section conductors as a function of their perimeter to area ratio at low (10 Hz), medium (1 MHz), and high (100 MHz) frequency signals. Inset shows current density maps for circular, square, and rectangular conductor cross-sectional geometries. **d** A flexible integrated circuit consisting of passive AC devices with high quality factor and sensitivity made from liquid metal conductors.

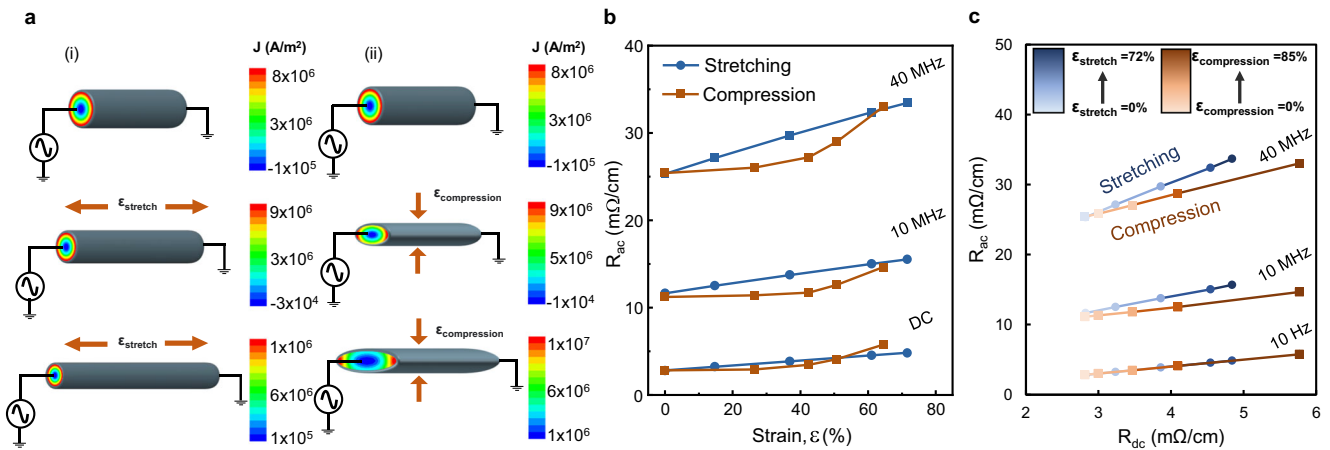
to their higher bulk resistivity compared to more conductive metals such as copper. In addition, because the skin depth scales inversely with frequency, it increases the effective resistance of metals for AC signal conduction by leading to current crowding at the surface. Liquid metal conductors, assembled by the printing or dispensing methods<sup>24</sup> with dimensions in the range of 100's  $\mu\text{m}$  to 1 mm, produce the onset of an increase in resistance at the 100s kHz–MHz range. At this point, the skin depth becomes considerably smaller than the diameter of the conductor. Figure 1a illustrates the difference in the current density between low frequency, medium frequency, and high-frequency signals, showing the severe current crowding at high frequencies and the evenly distributed current density at low frequencies, as calculated through finite element simulations.

Figure 1b shows the measured resistance as a function of frequency for liquid metal conductors of multiple diameters, illustrating how the AC skin effect enlarges the effective resistance at high frequencies. At a given frequency, the ratio of AC to DC resistance is amplified for the thicker liquid metal traces with mm-scale diameters, leading to an AC resistance that scales with  $f^{1/2}$  and can reach 10–100X of its DC value at 100 MHz. Interestingly, the larger diameter traces display the onset of the rise in the resistance at a lower frequency. The onset frequency of the skin effect-induced increase in resistance depends on the liquid metal geometry. It informs us whether the skin effect phenomenon will add to the resistance of our proposed AC mechanical sensors and whether it can limit the Q factor for liquid metal devices, such as an antenna used for wireless power transfer.

The most crucial geometrical consideration determining AC resistance from the skin effect is the ratio of the perimeter ('skin')

to the cross-sectional area. This is because the skin effect's influence largely depends on the complex interplay between the perimeter and area of the cross-section of the current-carrying conductor<sup>25,26</sup>. Figure 1c shows the trend of AC resistance for both the cross-section shape and the frequency. Here, we plot the simulated AC resistance of three different geometries typical of liquid metal circuits formed through methods such as soft lithography, including circular, square, and rectangular cross-sections with the same nominal area of  $4\text{ mm}^2$  but varying perimeter. Naturally, the circle has the lowest perimeter to area ratio, and the flatter rectangular cross-section has the highest perimeter to area ratio. The graph shows how, at high frequencies, the skin effect results in decreased AC resistance for conductors with a higher perimeter to area ratio, while at low frequencies ( $\sim\text{DC}$ ), the resistance is equivalent for all conductor shapes. The general implication of surface current crowding is that a conductor's cross-sectional shape will uniquely modulate the AC resistance and, therefore, provide additional sensitivity to mechanical deformation in the case of liquid metals. We will show how this phenomenon provides an opportunity for enhancing resistive sensing beyond the limits of DC transduction.

Figure 1d shows an example of a flexible circuit design including passive structures made from liquid metal, such as a spiral inductor and a serpentine patterned strain gauge. In the theoretical case of the spiral inductor, it is desirable to design for as low as possible an AC resistance to minimize losses and minimize its sensitivity to deformation for maintaining a tuned resonance (for example, in wireless power transfer<sup>22,27</sup>). However, for a strain gauge type mechanical sensor, the goal is to maximize the response to mechanical deformation<sup>28</sup>. This paper investigates



**Fig. 2 Simulated AC resistance of liquid metal conductors under stretching and compression.** **a** FEA simulations showing current density for stretching (i) and compression (ii) of a liquid metal sensor at 10 MHz with a 0.5 mm diameter. **b** Simulated AC resistance per cm for a 0.5 mm diameter as a function of both compressive and stretching strain for 10 Hz, 10 MHz, and 40 MHz. **c** A mapping of simulated  $R_{ac}$  and  $R_{dc}$  per cm for increasing degrees of compression and stretching at varied frequencies (10 Hz, 10 MHz, and 40 MHz).

this case of how to utilize AC excitation to amplify the sensitivity of liquid metal-based mechanical sensors, but the theory could equally be applied in reverse to minimize the sensitivity of tuned passive components to stretching deformation.

Our model system for investigating the physics of AC resistive sensing is a stretchable liquid metal wire encased in a compliant elastomeric tubing (PDMS). As the liquid metal-filled silicone tubes are mechanically deformed, the perimeter to area ratio varies with the two primary modes: pinching and stretching. As shown in Fig. 2a, this leads to distinct AC current density profiles predicted by 2D finite element electromagnetics simulations that can visualize the reverse current flowing in the core of the traces due to the skin effect. These maps show how the deformation of liquid metals into non-circular, ‘flatter’ elliptical cross-sections force current density onto the ends of the ellipse while stretching deformation (bottom) changes the effective diameter of the cross-section relative to the skin depth. With increasing compression, the perimeter to area ratio of the elliptical cross-section increases as the liquid metal is displaced. Along the major axis of the ellipse, the current crowds densely at the end lobes, which leads to a severe asymmetric skin effect as opposed to having a symmetrical current crowding in stretching modes. For instance, the peak current density ( $1.1 \times 10^7 \text{ A m}^{-2}$ ) of the highly orthogonally compressed elliptical cross-section is 3.5X higher than the current density of the circular cross-section ( $8 \times 10^6 \text{ A m}^{-2}$ ). However, due to the asymmetry in the mechanically-increased perimeter to area ratio for a flatter elliptical trace, the opposing eddy current at the center of a trace is weaker than the incoming input current than a symmetric cross-section akin to a circle. For example, as shown in the current maps in Fig. 2a, the current density ( $1.9 \times 10^5 \text{ A m}^{-2}$ ) at the center of the cross-section for a highly stretched (70%) trace is  $\sim 10\text{X}$  lower than the case of a highly compressed liquid metal trace ( $1.78 \times 10^6 \text{ A m}^{-2}$ ), denoting a weaker opposing current for a compressed trace than a stretched trace at the center. This results in more utilization of the center of a trace for carrying AC, making the trace less resistive. As a result, the  $R_{ac}$  change in a trace compressed out-of-plane by a normal force is much less intense than that of the stretched trace. Thus, mechanical strain modulates the AC resistance spectrum by modifying the current distribution, as shown in Fig. 2a, which can serve as a basis for transducing these mechanical strains at high frequencies.

Unlike DC sensing, AC resistive sensing provides sufficient information to sense *multimodal* mechanical deformation, distinguishing between forces applied in an orthogonal (compression) or parallel (stretching) axis to the direction of current flow.

Figure 2b illustrates the response of AC and DC resistance per unit length of a given liquid metal conductor to increasing degrees of stretching and compression deformation, as predicted by finite element analysis (FEA) simulations for excitation at DC, 10 MHz, and 40 MHz. The simulated response includes circular cross-sections with radius  $r_0$  compressed to a series of ellipses with increasing compression along the minor axis,  $b$ . An effective compression percentage can be calculated by normalizing the change in the minor axis by the initial radius ( $\frac{b-r_0}{r_0} \cdot 100\%$ ). Figure 2b also shows the result of compression from 0 to 84%, corresponding to the eccentricity of 0 to 0.95. The simulated liquid metal trace is stretched along its length from 0 to 71.6% tensile strain. With increasing strain, AC and DC resistance increase concurrently, as expected from the reduced cross-sectional area upon stretching (blue) and compression (orange). However, at high frequencies (10 MHz and 40 MHz), the change of  $R_{ac}$  due to stretching is much steeper than the change due to compression, which results from the asymmetric cross-section induced by compression. Moreover, DC resistance scales differently than AC resistance does with longitudinal strain. A simple analysis of DC resistance for a cylindrical geometry shows that the resistance scales with  $(1 + \epsilon)^2$ , where  $\epsilon$  is defined as the longitudinal strain<sup>29,30</sup>, induced by stretching in the axial direction. On the other hand, AC resistance is limited by the skin effect, trending with  $(1 + \epsilon)^{1.5}$ , a scaling law that can be derived by accounting for the current flow within one skin depth for AC signals in the same cylindrical geometry (see Supplementary Note 1, Supplementary Fig. 1).

Figure 2c displays a plot of  $R_{ac}$  as a function of  $R_{dc}$  for both increasing stretching and compression (with higher values of strain denoted by darker symbols) for different frequencies (10 Hz, 10 MHz, and 40 MHz). The advantage of using this mapping to a combination of  $R_{dc}$  and  $R_{ac}$  for respective deformation modes is that it can distinguish the ratio between AC and DC resistance for stretching and compression, visible in Fig. 2c as two non-intersecting lines. This distinguishability facilitates the process of tracking the degree and nature of the deformation of the sensor with accuracy while interfacing with readout circuitry. As seen from Fig. 2c, in compression, the ratio of changes in  $R_{ac}$  to  $R_{dc}$  is weaker than the change due to current crowding in the stretching mode. For example, at 10 MHz, the slope of the line representing the change of  $R_{ac}$  to  $R_{dc}$  for compression is 1.6X lower than stretching for the same nominal amount of strain. On the other hand, at low frequencies (10 Hz),  $R_{ac}$  and  $R_{dc}$  are both similar for stretching and compression, overlapping in the 2D  $R_{ac}$  vs.  $R_{dc}$

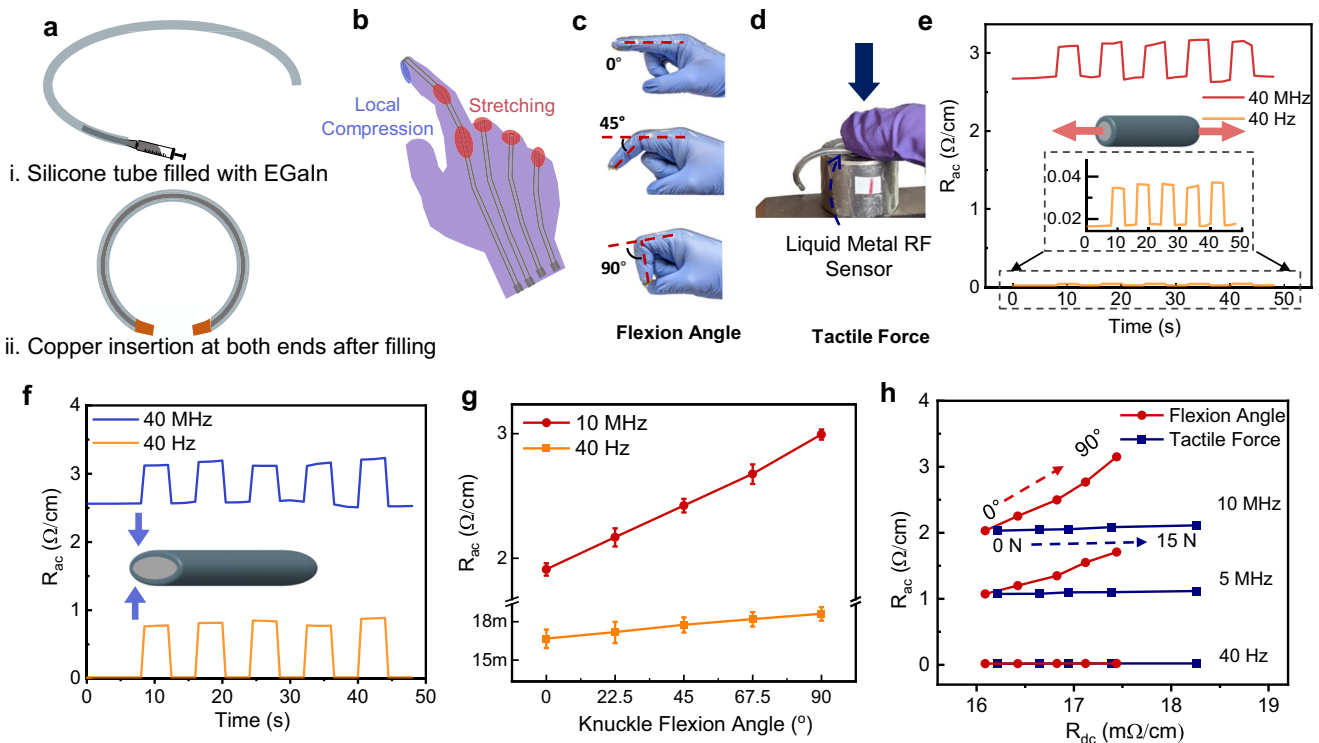


**Fig. 3 AC-enhanced mechanical sensor fabrication and gesture tracking.** **a** Fabrication scheme of the high-frequency liquid metal sensors. **b** Illustration highlighting compression and stretching zones located at the location of fingertips and knuckle joint in a liquid metal RF sensor-based gesture tracking glove. Pictures showing quantitative experimental measurements of stretching (**c**) and compression (**d**) via gesture tracking gloves. Resistance vs. time for dynamic cycles of stretching (**e**) and compression (**f**) in response to flexion of the knuckle joint angle ( $45^\circ$ ) and digital pinching force ( $\sim 20$  N) at low (40 Hz) and high frequency (40 MHz). Error bars denote  $\pm 1$  s.d. **(g)** AC resistance at high (10 MHz) and low frequency (40 Hz) as a function of knuckle flexion angles. **(h)**  $R_{ac}$  vs.  $R_{dc}$  map for different knuckle bending angle (red) and pinching force (blue) at the fingertip at different frequencies (10 MHz, 5 MHz, 40 Hz).

space. This means that DC transduction alone cannot distinguish between one deformation mode and another, for example, whether the  $\Delta R_0$  has resulted from a 20% stretch or a 15% compression. To summarize, we can see that a key feature of using both AC resistance and DC resistance is that, in combination, they are sensitive enough to identify both the modes and degree of deformation quantitatively.

### AC-enhanced gesture sensing

We fabricated gesture tracking gloves with mounting liquid metal sensors to demonstrate the utility of AC-enhanced resistive sensing. This facile fabrication method starts with filling a 10 cm long bare PDMS tube with an inner diameter of 0.5 mm with EGaIn and is followed by sealing the ends of the tube with copper terminations (see the experimental section for details). The fabrication method is exhibited in Fig. 3a. Figure 3b displays our design of a gesture tracking glove with strategically placed liquid metal sensors to monitor the stretching of the knuckle joint and pinching force applied at the fingertips. This sensing modality is well suited to implementation in wearable haptic systems because it allows a single liquid metal sensing element to detect multiple deformation modes, simplifying the design of a wearable readout circuit and facilitating multiplexing. Figure 3c depicts the stretching mode of deformation of the liquid metal sensor in response to flexion at the second knuckle of the index finger at multiple angles. Figure 3d shows the compression mode due to force stemming from the fingertip against a load cell of the force sensing system. Figure 3e, f demonstrates the liquid metal trace's AC and DC resistance during cyclic knuckle flexion and fingertip tactile force. As expected, progressively greater flexion or compressive tactile force increases both the AC and DC resistance.

Figure 3e, f also illustrates multiple cycles of flexion and compression via pinching to show the modulation of both AC and DC resistance over time, displaying the sensor's excellent reversible electromechanical nature with low hysteresis. Figure 3g demonstrates the ability of this AC-enhanced liquid metal sensor to quantitatively sense gestures through measurement of knuckle flexion angle from  $0^\circ$  to  $90^\circ$ . At progressively higher flexion angles, the stretching strain increases at the joint, which is reflected in the AC resistance at 10 MHz to a greater degree than at DC, illustrating the increased sensitivity achieved by utilizing the skin effect.

The AC-enhanced liquid metal sensor can distinguish between the varying force of touch or degree of finger flexion experimentally through a high-frequency excitation, as had been predicted by the FEA simulations. Simultaneous measurement of both AC and DC resistance provides the ability to distinguish gestures and tactile force, as shown in Fig. 3h. Figure 3h shows a map of AC (5 MHz and 10 MHz) and DC resistance measured for a single wearable liquid metal trace worn during bending and pressing gestures executed by the wearer's index finger. High-frequency (5 and 10 MHz) resistance measurements reliably differentiate these two classes of gestures, while DC measurements provide overlapping data that is indistinguishable. This unique capability will provide multifunctionality for liquid metal wearable sensors, specifically aiding force-feedback haptic systems<sup>31</sup> requiring both gestures and touch monitoring.

### Enhancing low-power respiratory sensing

Another significant result of AC strain sensing is that it can directly translate to power savings and reduced complexity for flexible readout circuits. This is particularly important for wearable systems with significant power and speed limitations, requiring high computational efficiency for performing onboard signal



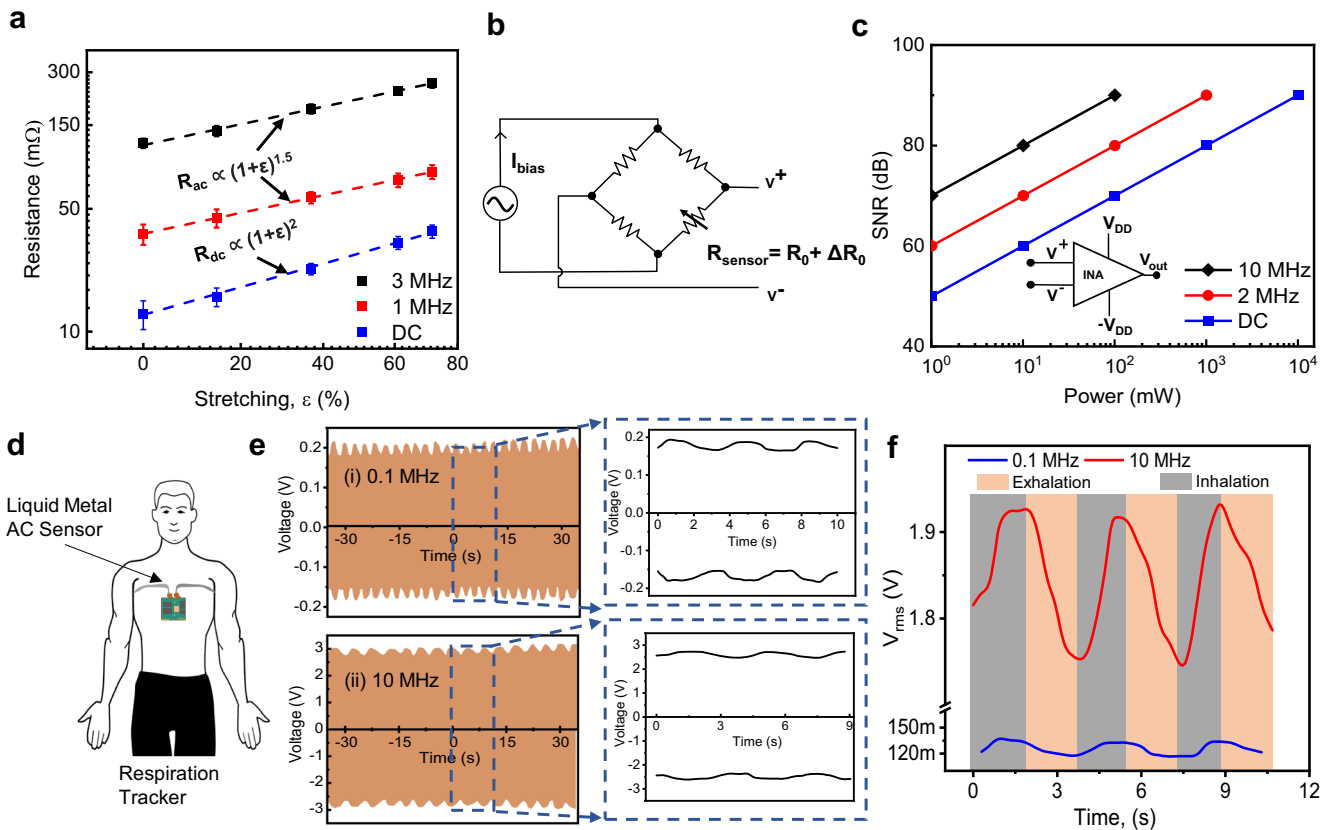


**Fig. 4 Modeling of experimental AC resistance and demonstration of a low-power respiratory tracker.** **a** Experimentally measured resistance during stretching and the predicted resistances from a mathematical model as a function of stretching at different frequencies (DC, 1 MHz, and 3 MHz) for a liquid metal wire with 1.5mm diameter. Error bars denote  $\pm 1$  s.d. **b** A Wheatstone bridge circuit incorporating the liquid metal sensor as  $R_{\text{sensor}}$ . **c** Simulated signal-to-noise ratio (SNR) as a function of power consumption from the bias current of the Wheatstone bridge at different excitation frequencies (DC, 2 MHz, and 10 MHz). An instrumentation amplifier, shown in the inset, is proposed to collect differential voltage measurements of the liquid metal sensor. **d** Liquid metal AC sensor-based system is placed on the human chest area to collect and process respiratory data. **e** AC signal as a function of time for (i) low frequency (0.1 MHz) and for (ii) high-frequency (10 MHz) input signal for breathing phases (exhalation and inhalation). **f**  $V_{\text{rms}}$  vs. time for corresponding breathing phases at low frequency (0.1 MHz) and high frequency (10 MHz).

processing with a low-power microcontroller (MCU)<sup>32</sup>. The improved readout capability of AC resistance-based sensors stems from two features: firstly, AC resistance has a more linear dependence on the strain, which is a desirable property for demodulating complex biomechanical signals with high resolution. Secondly, AC sensing requires substantially lower bias currents and delivers higher SNR. Figure 4a depicts the experimental resistance as a function of stretching strain as well as the regression model fits according to scaling laws (see Supplementary Note 1), showing the resistance change with strain at different frequencies (DC, 1 MHz, and 3 MHz). For DC, a quadratic regression model with a dependence on  $(1 + \epsilon)^2$  yields a tight fit with the measured resistance values. This also means that the gauge factor itself is linearly changing with strain for DC resistive sensing, degrading the sensor linearity for a given range of strains. For the high-frequency resistance, the regression model fits the data well with a  $(1 + \epsilon)^{1.5}$  dependency and the trend shown in Fig. 4a illustrates the improved linearity of AC resistive sensing. In the case of compressive strain, a mathematical model for elliptical cross-section conductors found in literature<sup>25</sup> fits the simulated  $R_{\text{ac}}$  properly with the changing ratio of the major (a) to the minor axis (b) in response to compression. Supplementary Figure 2 displays the fit between the  $R_{\text{ac}}$  for 10 MHz from the mathematical equation and the simulation, which shows a linear dependency on  $\ln(a/b)$ . We also note that the experimentally measured AC resistance for stretching and compression normalized per length

matches the simulations shown in Fig. 2. The agreement between the simulation model and experimental results is displayed in Supplementary Fig. 4.

AC measurements are well suited to high accuracy and low-power detection because they can reduce pickup of random  $1/f$  noise, as has been previously noted for performing impedance measurements<sup>33</sup>. The skin effect enhanced AC resistance has the additional benefit of directly reducing the power consumption for a nominal liquid metal strain sensor by increasing the nominal resistance. To illustrate this point, we can assume that the sensor is connected in a typical Wheatstone bridge configuration as one of the four arms with a matched nominal resistance,  $R_0$ , as shown in Fig. 4b. The differential voltage measured across the sensing resistance is generated by passing a sufficient bias current through the bridge. Therefore, the differential voltage must be substantially larger than the nominal noise voltage ( $V_N$ ) at the instrumentation amplifier's (INA) input terminals. This ratio can be considered a nominal signal-to-noise ratio (SNR) for a resistive sensing measurement. Figure 4c depicts the scaling of the SNR with power consumption from the bias current applied to the bridge circuit. Using a 10 MHz signal alone can reduce power consumption by 100X for a liquid metal sensor with a nominal DC resistance of  $1 \Omega$ , eliminating the need for additional readout circuit complexity (for derivation, see Supplementary Note 2) and reducing the potential for sensor drift from self-heating effects. We also note that power consumption scales linearly for an array

of sensors, enforcing a strict tradeoff for high SNR measurements in low-power systems, making the usage of high-frequency excitation even more critical<sup>34</sup>.

Furthermore, DC excitation-based systems suffer from thermo-electric offset voltage when interconnecting the sensory unit to the signal conditioning unit<sup>35,36</sup>. This thermoelectric offset is usually amplified when connected to an INA, altering the accuracy and measurement range of the sensor system. The proposed liquid metal sensor is free of such effect as it takes advantage of using AC excitation and keeps the measurement range unperturbed. Furthermore, any fluctuations in temperature for our AC sensors are partially mitigated due to the weaker dependence of AC resistance on temperature compared with DC resistance.

We fabricated a respiratory tracker based on liquid metal traces to illustrate how the AC-enhanced sensing principle can improve signal intensity. This tracker is placed on the chest area of the human body, as depicted in Fig. 4d, with a thin elastic liquid metal sensor wrapping around the user's torso. The sensor is excited while measuring the voltage drop across the sensor's AC resistance during the exhalation and inhalation phases of breathing. As the sensor is stretched due to the rib cage's expansion during inhalation, the resistance increases, and so does the voltage across the sensor's resistance. Figure 4e shows two oscilloscope traces and the extracted voltage envelope from these readings, which are amplitude modulated through breathing phases at low (100 kHz) and high (10 MHz) frequencies. Thanks to the enhanced resistance due to the skin effect, using a higher frequency current enables a substantially larger output voltage across the liquid metal sensor. Figure 4f depicts the extracted root-mean-square voltage for that modulated envelope for a few cycles of exhalation and inhalation. In this case, the skin effect is responsible for enhancing the SNR of approximately 24 dB for this respiratory measurement, while power consumption was simultaneously reduced by 6.6X for an equivalent bias current.

To put our AC-enhanced liquid metal sensor in context, Supplementary Table 1 presents a summary comparing our work with other AC-based liquid metal sensors implemented for the detection of mechanical stimuli. Compared with GHz range time-domain reflectometry<sup>14</sup>, our MHz range resistive sensing mode could allow for simpler readout circuits and the potential for smaller, high-resolution sensor arrays. In contrast to other reports of capacitive liquid metal sensors<sup>17</sup>, our method also allows the distinction and quantification of multiple stimuli by monitoring both the DC and AC impedance. Based on these prior works, we also highlight the clear opportunity for future liquid metal sensors to simultaneously use both the real and reactive components of impedance to improve accuracy, enhance dynamic range, and expand the range of sensing modalities.

In summary, we demonstrate a method for AC-enhanced resistive mechanical sensing that leverages the deformability of liquid metals to achieve low-power detection of mechanical stimuli in wearable electronics. Finite element simulations are presented to illustrate the mapping between the deformation of a liquid metal conductor's cross-sectional geometry and its AC resistance. Experimental measurements confirm these results in the 40 Hz to 100 MHz range, illustrating how multiple modes of mechanical stimuli (out-of-plane compression or in-plane stretching) can be distinguished and quantified in a liquid metal trace acting as a sensor, matching a compact mathematical model to predict the resistance as a function of strain. We finally demonstrate this principle in two wearable biomedical devices, first with the liquid metal sensor mounted on a glove and second with the sensor mounted on a chest band for respiratory tracking. These demonstrations provide a view of how AC-enhanced sensing can improve the power consumption and sensitivity of RF-based haptic electronic systems for future augmented or virtual reality devices. We expect that other manifestations of eddy current, such as the proximity effect (induction of eddy current in

nearby conductors), can also be used to sensitively modulate the AC resistance. Based on these findings, the strategic use of new device geometries and specific designs for a given frequency range promises to extend sensing functionalities for versatile tactile sensing of touch, shear force, and torsion.

## METHODS

### Liquid metal sensor fabrication

The liquid metal sensors were fabricated by filling PDMS tubing with EGaln via a needle-tipped syringe. The needle's inner diameter was selected to be slightly larger than the tube's diameter so that the PDMS tube tightly fits over the nozzle. This arrangement helps the liquid metal flow so that the meniscus of the liquid metal encompasses the whole cross-section of the tube, leaving no air bubbles. Cylindrical copper wires inserted at both ends of the PDMS tube were used as rigid contact points for high-frequency electrical measurements. The Cu wire diameter was selected to be approximately 50% larger than the PDMS diameter so that the PDMS tube is tightly wrapped around the metal at the junction of the copper wire and the PDMS tube. Adhesive (KG92548R) was placed to seal the junction further to prevent any liquid metal from leaking.

A respiratory tracker was also built by the same fabrication scheme. The length of the tracker was long enough (100 cm) to wrap a medium-built human chest one time. The diameter of the tube was chosen to be the smallest (0.5 mm) we could find off-the-shelf so that the DC resistance (1.4  $\Omega$ ) of the sensor is comparable to the output impedance (50  $\Omega$ ) of the wavefunction generator. In this way, the low-frequency voltage output measurement from the sensor could be done by the oscilloscope with an acceptable noise margin.

### FEA simulation of high-frequency electrical properties

Finite element electromagnetic simulations were performed using the ANSYS Maxwell simulator package. The simulation was done on a liquid metal-filled tube cross-section where 2D Maxwell equations are applied. The excitation AC was set to be 1 A for different geometrical configurations of the EGaln filled tube. The resultant eddy current map and the related resistance value were calculated through the FEA solver. Different ranges of frequency points, from 10 Hz to 100 MHz, were performed for the eddy current analysis alongside their corresponding current maps. The simulations were done with a 0.1% error with 30 iterations and simulator-assisted fine meshing.

The cross-section tends towards a more elliptical shape with additional orthogonal compressive strain to the length. The values for the major and minor axes (a, b) were found by taking the cross-sectional images of compressively strained blank PDMS tubes. The PDMS tube was mounted on a load cell of the Pasco Materials Testing System (ME-8244), and the vertical displacement of the load cell, which compressed the PDMS tube, was recorded through the PASCO interface. As Supplementary Fig. 3 shows, cross-sectional images display a progressive trend in increasing the eccentricity of the ellipses with vertical displacement of the load cell. ImageJ was used to process the image to get the deformed tube's major and minor axis at each strain value. These changes in axis values are in accord with the displacement value from the PASCO's vertical displacement value. These axis values were used later to simulate the equivalent ellipse in the FEA simulator to mimic the compressive strain. To replicate the uniaxial stretching with a liquid metal sensor in ANSYS, we simulated tubes with different diameters that reflected the length increment while stretching was performed.

### AC measurements of liquid metal conductors

AC impedance measurements were completed with an Agilent 4294A impedance analyzer. AC resistances were recorded from 40 Hz to 110 MHz. Open, short, and fixed resistance calibrations were performed for the entire frequency range. We specifically note that the AC resistance of the copper terminations is calibrated out while doing the short calibration. Our measurements of the AC liquid metal sensors were taken from 10 Hz up to approximately 5 MHz over which the agreement between experimental and simulated resistance was very close, as shown in Supplementary Fig. 5. Above 10 MHz, the self-resonance of the measurement probe setup (Supplementary Fig. 5) made accurate extraction of the real component of the impedance more challenging. The use of a custom, rigid test fixture would allow more precise calibration and deembedding of parasitics for

measurements in the 10–100 MHz range and above. The PASCO mechanical measurement system was used concurrently during the AC electrical measurements to provide control over the compression of the sensor for a range of 0 to 85%, measured from compression of the minor axis value compared to the starting radius of the circle. In addition, a custom-built uniaxial stretching setup was created for the stretching test of the sensor from 0 to 70% strain.

For the respiratory tracker measurement, a waveform generator (Agilent 33521A) was used to excite the sensor with sine waves with two different frequencies (100 kHz and 10 MHz) but with the same peak-to-peak voltage (5 V). An Agilent DSO6032a was attached to the sensor to get the wave envelope while the sensor was connected to the waveform generator. The screen-grab tool was used to reconstruct the amplitude-modulated waveforms during the experiment.

## DATA AVAILABILITY

All relevant simulation and experimental data that are generated and analyzed for this study are available from the corresponding author (william.j.scheiderer@dartmouth.edu) upon request.

Received: 13 April 2022; Accepted: 24 July 2022;

Published online: 09 August 2022

## REFERENCES

- Jeong, Y. R. et al. Highly stretchable and sensitive strain sensors using fragmented graphene foam. *Adv. Funct. Mater.* **25**, 4228–4236 (2015).
- Lochner, C. M., Khan, Y., Pierre, A. & Arias, A. C. All-organic optoelectronic sensor for pulse oximetry. *Nat. Commun.* **5**, 5745 (2014).
- Jose, M., Lemmens, M., Bormans, S., Thoelen, R. & Deferme, W. Fully printed, stretchable and wearable bioimpedance sensor on textiles for tomography. *Flex. Print. Electron.* **6**, 015010 (2021).
- Kwon, S. et al. Skin-conformal, soft material-enabled bioelectronic system with minimized motion artifacts for reliable health and performance monitoring of athletes. *Biosens. Bioelectron.* **151**, 111981 (2020).
- Zhu, Z., Li, R. & Pan, T. Imperceptible epidermal–iontronic interface for wearable sensing. *Adv. Mater.* **30**, 1705122 (2018).
- Wang, Q., Yu, Y. & Liu, J. Preparations, characteristics and applications of the functional liquid metal materials. *Adv. Eng. Mater.* **20**, 1700781 (2018).
- Yoon, J. et al. Design and fabrication of novel stretchable device arrays on a deformable polymer substrate with embedded liquid-metal interconnections. *Adv. Mater.* **26**, 6580–6586 (2014).
- Rahman, M. S. & Grau, G. Direct writing of stretchable metal flake conductors: improved stretchability and conductivity by combining differently sintered materials. *Flex. Print. Electron.* **5**, 025005 (2020).
- Matsuzaki, R. & Tabayashi, K. Highly stretchable, global, and distributed local strain sensing line using gain electrodes for wearable electronics. *Adv. Funct. Mater.* **25**, 3806–3813 (2015).
- Majidi, C., Kramer, R. & Wood, R. J. A non-differential elastomer curvature sensor for softer-than-skin electronics. *Smart Mater. Struct.* **20**, 105017 (2011).
- Dorsey, K. L. & Lazarus, N. Lifetime of liquid metal wires for stretchable devices. *Adv. Mater. Technol.* **6**, 2001100 (2021).
- Wessendorf, A. M. & Newman, D. J. Dynamic understanding of human-skin movement and strain-field analysis. *IEEE Trans. Biomed. Eng.* **59**, 3432–3438 (2012).
- Wu, Y. et al. Liquid metal fiber composed of a tubular channel as a high-performance strain sensor. *J. Mater. Chem. C* **5**, 12483–12491 (2017).
- Leber, A. et al. Soft and stretchable liquid metal transmission lines as distributed probes of multimodal deformations. *Nat. Electron.* **3**, 316–326 (2020).
- Lazarus, N., Meyer, C. D., Bedair, S. S., Nochetto, H. & Kierzewski, I. M. Multilayer liquid metal stretchable inductors. *Smart Mater. Struct.* **23**, 085036 (2014).
- Cooper, C. B. et al. Stretchable capacitive sensors of torsion, strain, and touch using double helix liquid metal fibers. *Adv. Funct. Mater.* **27**, 1605630 (2017).
- Yang, J. et al. Ultrasoft liquid metal elastomer foams with positive and negative piezopertivity for tactile sensing. *Adv. Funct. Mater.* **30**, 2002611 (2020).
- Varga, M., Ladd, C., Ma, S., Holbery, J. & Tröster, G. On-skin liquid metal inertial sensor. *Lab. Chip* **17**, 3272–3278 (2017).
- Kim, M., Alrowais, H., Pavlidis, S. & Brand, O. Size-scalable and high-density liquid-metal-based soft electronic passive components and circuits using soft lithography. *Adv. Funct. Mater.* **27**, 1604466 (2017).
- Guo, L. & DeWeerth, S. P. High-density stretchable electronics: toward an integrated multilayer composite. *Adv. Mater.* **22**, 4030–4033 (2010).
- Lu, T., Wissman, J., Ruthika & Majidi, C. Soft anisotropic conductors as electric vias for ga-based liquid metal circuits. *ACS Appl. Mater. Interfaces* **7**, 26923–26929 (2015).
- Jeong, Y. R. et al. A skin-attachable, stretchable integrated system based on liquid GaInSn for wireless human motion monitoring with multi-site sensing capabilities. *NPG Asia Mater.* **9**, e443 (2017).
- Lamb, H. & Glaisher, J. W. L. XIII. On electrical motions in a spherical conductor. *Philos. Trans. R. Soc. Lond.* **174**, 519–549 (1883).
- Votzke, C., Daalkhajav, U., Mengüç, Y. & Johnston, M. L. 3D-printed liquid metal interconnects for stretchable electronics. *IEEE Sens. J.* **19**, 3832–3840 (2019).
- Morgan, V. T. The current distribution, resistance and internal inductance of linear power system conductors—a review of explicit equations. *IEEE Trans. Power Deliv.* **28**, 1252–1262 (2013).
- Cockcroft, J. D. Skin effect in rectangular conductors at high frequencies. *Proc. R. Soc. Lond. Ser. Contain. Pap. Math. Phys. Character* **122**, 533–542 (1929).
- Yamagishi, K., Zhou, W., Ching, T., Huang, S. Y. & Hashimoto, M. Ultra-deformable and tissue-adhesive liquid metal antennas with high wireless powering efficiency. *Adv. Mater.* **33**, 2008062 (2021).
- Pang, C. et al. A flexible and highly sensitive strain-gauge sensor using reversible interlocking of nanofibres. *Nat. Mater.* **11**, 795–801 (2012).
- Gao, Q. et al. Microchannel structural design for a room-temperature liquid metal based super-stretchable sensor. *Sci. Rep.* **9**, 5908 (2019).
- Chen, J. et al. Superelastic, sensitive, and low hysteresis flexible strain sensor based on wave-patterned liquid metal for human activity monitoring. *ACS Appl. Mater. Interfaces* **12**, 22200–22211 (2020).
- Oh, J. et al. A liquid metal based multimodal sensor and haptic feedback device for thermal and tactile sensation generation in virtual reality. *Adv. Funct. Mater.* **31**, 2007772 (2021).
- Huang, Y. et al. Liquid metal-based epidermal flexible sensor for wireless breath monitoring and diagnosis enabled by highly sensitive Sn<sub>2</sub> nanosheets. *Research* **2021**, 984728 (2021).
- Corcoran, J. & Nagy, P. B. Compensation of the skin effect in low-frequency potential drop measurements. *J. Nondestruct. Eval.* **35**, 58 (2016).
- Ahmad, M., Malik, S., Patel, H. & Baghini, M. S. A portable low-voltage low-power ppm-level resistive sensor measurement system. *IEEE Sens. J.* **22**, 2338–2346 (2022).
- Fraden, J. In *Handbook of Modern Sensors: Physics, Designs, and Applications* (Fraden, J. ed.) 1–12 (Springer, 2010).
- Ahmad, M. et al. An auto-calibrated resistive measurement system with low noise instrumentation ASIC. *IEEE J. Solid-State Circuits* **55**, 3036–3050 (2020).

## ACKNOWLEDGEMENTS

The authors owe our gratitude to Professor Charlie Sullivan for his helpful advice and training to use the impedance analyzer. A.B.H. was supported by a National Science Foundation Graduate Research Fellowship. M.S. Rahman was supported by Dartmouth's PhD Innovation Fellowship.

## AUTHOR CONTRIBUTIONS

The manuscript was written with the contributions of all authors. All authors have approved the final version of the manuscript. W.J.S. and M.S.R. conceived the concept of the project. W.J.S. supervised the project. W.J.S. and M.S.R. wrote the manuscript. M.S.R. simulated, fabricated, and characterized the sensor. J.E.H. and A.B.H. assisted in the writing and editing of the manuscript.

## COMPETING INTERESTS

The authors declare no competing interests.

## ADDITIONAL INFORMATION

**Supplementary information** The online version contains supplementary material available at <https://doi.org/10.1038/s41528-022-00206-3>.

**Correspondence** and requests for materials should be addressed to William J. Scheiderer.

**Reprints and permission information** is available at <http://www.nature.com/reprints>

**Publisher's note** Springer Nature remains neutral with regard to jurisdictional claims in published maps and institutional affiliations.



**Open Access** This article is licensed under a Creative Commons Attribution 4.0 International License, which permits use, sharing, adaptation, distribution and reproduction in any medium or format, as long as you give appropriate credit to the original author(s) and the source, provide a link to the Creative Commons license, and indicate if changes were made. The images or other third party material in this article are included in the article's Creative Commons license, unless indicated otherwise in a credit line to the material. If material is not included in the article's Creative Commons license and your intended use is not permitted by statutory regulation or exceeds the permitted use, you will need to obtain permission directly from the copyright holder. To view a copy of this license, visit <http://creativecommons.org/licenses/by/4.0/>.

© The Author(s) 2022